# Precisely Controlled Synthesis of Hybrid Intermetallic−Metal Nanoparticles for Nitrate Electroreduction

Jiaqi Yu, Anna F. Kolln, Dapeng Jing, Jinsu Oh, Hengzhou Liu, Zhiyuan Qi, Lin Zhou, Wenzhen Li, and Wenyu Huang*

Read Online

ACCESS | Metrics & More | Article Recommendations | SI Supporting Information

**ABSTRACT:** Precisely controlled synthesis strategies to prepare anisotropic nanomaterials with high yield and easy operation are exceedingly in demand because hybrid structures often introduce novel properties that cannot be achieved by isotropic nanomaterials. Here, a one-pot, two-step hot injection method was developed to prepare $Cu_6Sn_5$−Sn hybrid intermetallic−metal nanoparticles with an anisotropic structure. Hybrid nanoparticles with distinguishable Sn and $Cu_6Sn_5$ domains were formed under mild temperature. Different compositions of Sn and $Cu_6Sn_5$, ranging from pure Sn to various ratios of the Sn part and $Cu_6Sn_5$ part to pure $Cu_6Sn_5$, were achieved by modulating the reaction conditions, the ratio of the two metals. The as-synthesized asymmetric $Cu_6Sn_5$−Sn nanoparticles show small onset potentials (0.2 V vs reversible hydrogen electrode, RHE) and high activities (1125 mA $mg^{-1}_{metal}$ at −0.2 V vs RHE) in electrocatalytic nitrate reduction reaction. Unlike reported Cu- or Sn-based catalysts in nitrate reduction, the hybrid $Cu_6Sn_5$−Sn nanoparticles selectively produce the unstable intermediate, nitrite, within a wide reduction potential window.

**KEYWORDS:** anisotropic nanoparticles, intermetallic compounds, one-pot synthesis, electrocatalysis, nitrite
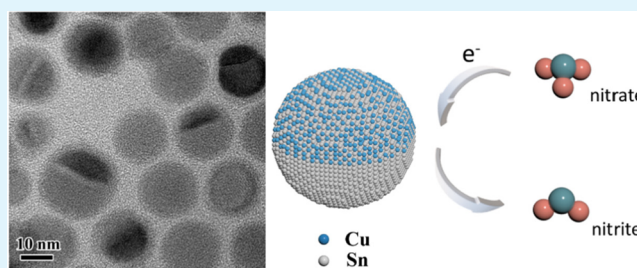
## INTRODUCTION

Anisotropic nanomaterials have attracted increasing interest because of their unique physical and chemical properties and wide applications across many fields, such as catalysis,[1−4] biomedicine,[5−7] and spectroscopy.[8,9] One type of anisotropic nanomaterials, hybrid nanomaterials that consist of two or more different components or structures, have won significant attention on their preparation, properties, and applications. Precisely controlled synthesis of hybrid nanomaterials has been developed for over a decade. Several synthetic methods, for example, phase separation,[10] template assisting,[11] and microfluidics,[12] have been reported. However, these reported methods usually involve complicated procedures or special instruments, resulting in relatively low yield and limited large-scale applications. To overcome these challenges, numerous efforts have been devoted to designing and developing strategies for synthesizing hybrid nanomaterials. For example, Li and co-workers reported an island nucleation and growth approach to preparing dual-component Janus mesopore silica nanoparticles (NPs) and studied their application on bimodal triggered drug delivery.[13] The island nucleation method was extended to prepare Janus metal−mesopore silica NPs for self-assembly and surface-enhanced Raman spectroscopy (SERS) studies.[14] These synthetic systems demonstrate the preparation of the anisotropic nanomaterials without performing complex synthesis procedures. However, the island nucleation is limited to certain compositions, in this case, the periodic mesoporous organosilica (PMO). Recently, the preparation of more than a hundred heterogeneous metal sulfide nanorods with complicated structures was realized via a cation exchange method.[15] Although this report illustrates a general strategy to synthesize hybrid materials, the preparation is restricted to metal sulfates. Therefore, the synthesis of hybrid nanomaterials with advanced structures through a precisely controllable and concise synthetic approach remains to be discovered.

Intermetallic compounds, the metal alloys with defined stoichiometries and ordered crystal structures, have been studied as attractive alternatives for many catalytic reactions, including hydrogenation and dehydrogenation reactions, because of their enhanced activity and stability over pure metals.[16,17] For instance, the non-precious metal intermetallic compound, $Cu_3Sn/Cu_6Sn_5$ supported on Cu foam, shows good catalytic activity in carbon dioxide electroreduction reaction to produce formate, with a faradaic efficiency of 82% and current density of 18.9 mA $cm^{-2}$ at −1.0 V vs reversible hydrogen
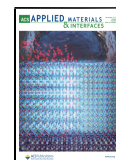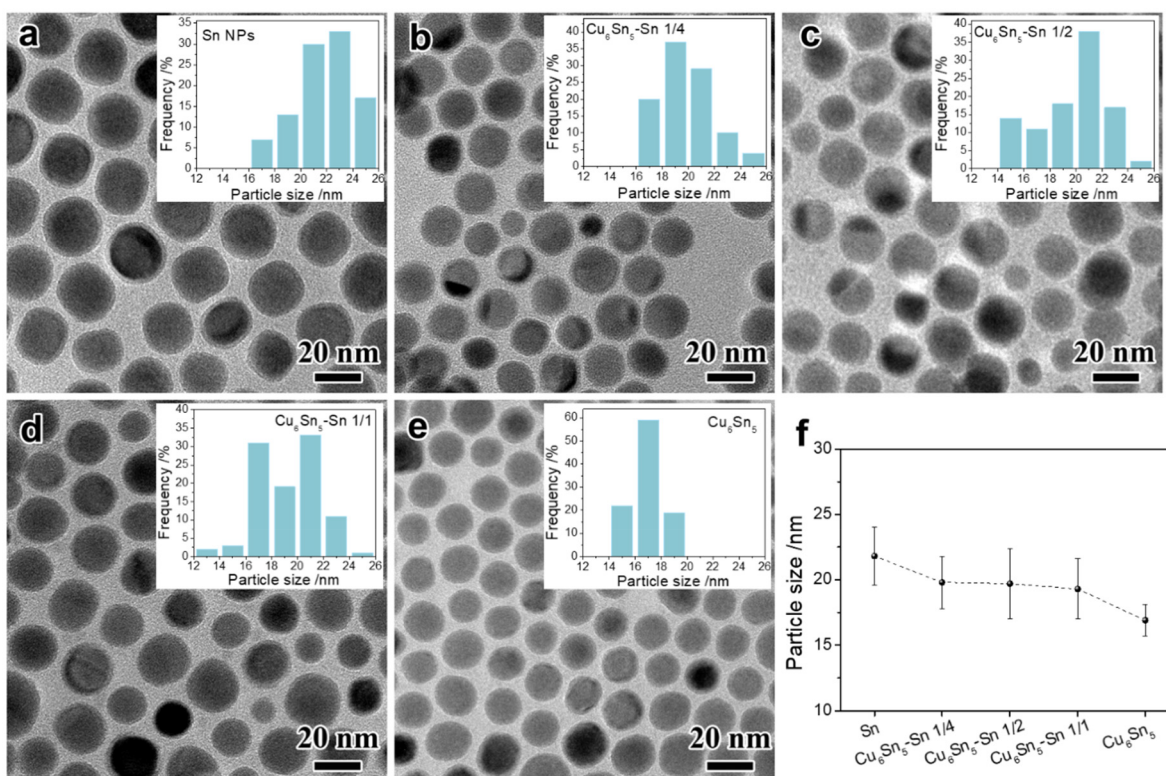
**Figure 1.** TEM images of (a) Sn, (b) hybrid $Cu_6Sn_5$−Sn 1/4, (c) hybrid $Cu_6Sn_5$−Sn 1/2, (d) hybrid $Cu_6Sn_5$−Sn 1/1, and (e) $Cu_6Sn_5$ NPs. The insets in a−e are the corresponding histograms of particle size distributions. (f) Plot of particle size vs nanoparticle with increasing Cu/Sn ratios.

electrode (RHE).[18] The dominant approach to synthesis intermetallic compound nanomaterials involves the impregnation of metal precursors on support materials followed by high-temperature annealing (typically over 500 °C) to form ordered intermetallic phases.[19] Because of the rapid atom diffusion during the high-temperature annealing, the preparation of anisotropic or hybrid nanomaterials is limited.

Herein, we developed a one-pot, two-step hot injection method for the precisely controlled synthesis of $Cu_6Sn_5$−Sn intermetallic−metal hybrid NPs. The components of $Cu_6Sn_5$−Sn hybrid NPs are tunable from pure Sn NP to intermetallic $Cu_6Sn_5$ cap/hemisphere on Sn structure and pure phase $Cu_6Sn_5$. The as-synthesized hybrid $Cu_6Sn_5$−Sn NPs show interesting catalytic properties in the electroreduction of nitrate. Unlike the reported Cu- and Sn-based catalysts that produce ammonia or nitrogen as the major products in nitrate electroreduction,[20−23] hybrid $Cu_6Sn_5$−Sn NPs selectively catalyze the production of nitrite. Nitrite has broad applications in chemical and pharmaceutical industries, participating in the production of nitroso and isonitroso compounds, caffeine, and agricultural pesticides.[24] However, nitrite can be easily reduced to more stable nitrogen species and is usually considered as the intermediate in the nitrate electroreduction reaction.[25] In addition to the uncommon reduction product, the hybrid $Cu_6Sn_5$−Sn NPs also show extraordinary activity in nitrate electroreduction with mass activity reaching 1125 mA $mg^{-1}_{metal}$ at −0.2 V vs RHE. The remarkable catalytic performance of hybrid $Cu_6Sn_5$−Sn NPs indicates that the anisotropic structure considerably influences the properties. The developed synthetic strategy could be extended to prepare other anisotropic intermetallic−metal or intermetallic−intermetallic nanomaterials.

## RESULTS AND DISCUSSION

The hybrid $Cu_6Sn_5$−Sn NPs were synthesized through a one-pot, two-step method. The Sn NPs were synthesized in an oleylamine (OAm) system.[26] After Sn NPs were formed, a $Cu(acac)_2$/OAm solution was injected into the solution, and the mixture was kept at 120 °C for 1 h before collecting the $Cu_6Sn_5$−Sn NPs. To prevent the oxidation of Cu and Sn, we applied Ar protection during the synthesis. The ratio between $Cu_6Sn_5$ and Sn was tuned by precisely controlling the injected amount of Cu precursor. The as-synthesized nanoparticles were named as Sn, hybrid $Cu_6Sn_5$−Sn $x/y$ ($x/y$ stands for the feeding ratio of Cu/Sn), and $Cu_6Sn_5$ for pure Sn, hybrid $Cu_6Sn_5$ with Sn, and pure phase intermetallic $Cu_6Sn_5$ NPs, respectively.

Transmission electron microscope (TEM) was used to characterize the morphology and structure of as-synthesized NPs. As shown in Figure 1, all NPs show a uniform spherical morphology in the TEM images of Sn and bimetallic NPs with different Cu/Sn ratios. The size of NPs for each sample was obtained by randomly measuring 100 particles. The average diameter of Sn NPs is 21.8 ± 2.2 nm. The diameters of two Sn-rich NPs, $Cu_6Sn_5$−Sn 1/4 and $Cu_6Sn_5$−Sn 1/2, are around 20 nm (19.8 ± 2.0 nm for $Cu_6Sn_5$−Sn 1/4 and 19.8 ± 2.7 nm for $Cu_6Sn_5$−Sn 1/2). The diameter of $Cu_6Sn_5$−Sn 1/1 and $Cu_6Sn_5$ NPs are 19.3 ± 2.3 and 16.9 ± 1.2 nm, respectively. The particle size change with the amount of Cu precursor added was plotted in Figure 1f. The addition of Cu to form the $Cu_6Sn_5$ intermetallic phase should result in an increased diameter of NPs if Sn is not consumed during the synthesis. However, the trend shown in the plot suggests that the particle size decreases with the incremental changes in the Cu amount, which can be explained by the replacement of Sn with Cu. For

the hybrid NPs, $Cu_6Sn_5$–Sn 1/4 NPs, $Cu_6Sn_5$–Sn 1/2 NPs, and $Cu_6Sn_5$–Sn 1/1 NPs, the anisotropic structure was confirmed by TEM images, showing as the combination of darker and lighter caps or hemispheres in a single particle (Figure 1b–d). Because of the different orientations of the NPs on the TEM grid and the 2D projection nature of TEM images, not all the anisotropic NPs present sections with different contrasts. The 3D model exhibits the projection of hybrid $Cu_6Sn_5$–Sn NPs from different directions, shown in Scheme S1. As shown in the scheme, the particle viewed from the top, representing $Cu_6Sn_5$ side of the hybrid particles, is homogeneous. Due to the combined effect of Z contrast and the diffraction contrast in the conventional TEM, directly identifying Sn or $Cu_6Sn_5$ domains by their contrast is insuperable. With the increase in Cu/Sn ratio, the hybrid $Cu_6Sn_5$–Sn NPs change from two unequally separated segments to two similar-sized hemispheres, shown in Figure 1b, c qualitatively. This component change with the different Cu/Sn ratios agrees with XRD and ICP results, which will be discussed later.

The crystal structure of NPs was characterized by powder X-ray diffraction (PXRD). From the PXRD patterns (Figure 2),
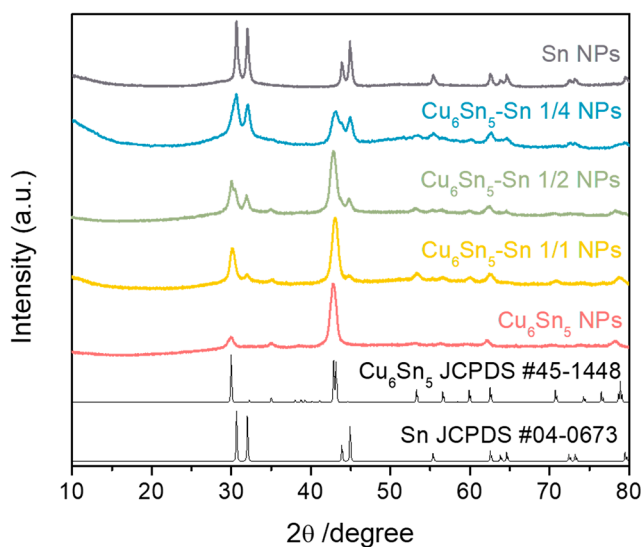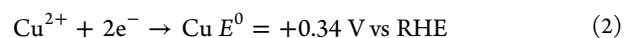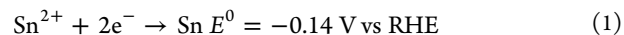


**Figure 2.** PXRD pattern of Sn, hybrid $Cu_6Sn_5$–Sn, and $Cu_6Sn_5$ NPs.

the as-synthesized Sn NPs has a $\beta$-Sn structure without any detectable tin oxides. The peaks at ∼43° from the hybrid $Cu_6Sn_5$–Sn and $Cu_6Sn_5$ NPs indicate the formation of the $Cu_6Sn_5$ intermetallic phase. The peak intensities of the $Cu_6Sn_5$ phase increased with more Cu precursors added during the synthesis, which suggests that the $Cu_6Sn_5$ portion in the NPs increases. For the hybrid $Cu_6Sn_5$–Sn 1/4 NPs, the PXRD pattern still shows a Sn-dominated structure. When the Cu/Sn ratios increase to 1/2 and 1/1, the $Cu_6Sn_5$ phase is paramount. The NPs show a pure $Cu_6Sn_5$ phase without any other detectable phases when further increasing the Cu/Sn ratio to 2/1. The PXRD results are consistent with the TEM images that the hybrid $Cu_6Sn_5$–Sn NPs have an anisotropic structure combining $Cu_6Sn_5$ intermetallic and Sn phases. Increasing the Cu/Sn ratio leads to an increase in the $Cu_6Sn_5$ intermetallic phase.

A detailed study of the hybrid $Cu_6Sn_5$–Sn NPs structure was performed through the high-resolution TEM (HR-TEM)

images and energy-dispersive spectroscopy (EDS) mapping analysis. As shown in Figure S1, Sn distributes in the whole hybrid $Cu_6Sn_5$–Sn NPs, whereas Cu only exists in half of the particles, which proves the anisotropic $Cu_6Sn_5$–Sn (half $Cu_6Sn_5$-half Sn) structure. In the pure phase $Cu_6Sn_5$ NPs, both Cu and Sn are uniformly distributed. The structure of hybrid $Cu_6Sn_5$–Sn NPs was further characterized by HR-TEM (Figure 3). The zone axis of $Cu_6Sn_5$ part is [−75−4], and the zone axis of Sn part is [010]. The lattice fringes of the top half are 2.99 and 3.00 Å, which correspond to the (−113) and (22−1) planes in the $Cu_6Sn_5$ crystal, whereas the lattice fringes of the bottom part are 2.76 and 2.84 Å, which correspond to the (200) and (101) planes in the Sn crystal. The crystallographic orientation relationship between the two phases is $[22−1]_{Cu6Sn5}//[−101]_{Sn}$. The crystal grain boundary between $Cu_6Sn_5$ and Sn phases in hybrid $Cu_6Sn_5$–Sn NPs should have minimal lattice mismatch and low interfacial energy.[27]

The elemental composition of the Cu–Sn NPs was analyzed by inductively coupled plasma-mass spectrometry (ICP-MS). The actual Cu/Sn ratio increases with the increase in the Cu/Sn feeding ratio (Figure S2). The actual Cu/Sn ratio is 0.25, 0.36, 0.57, and 1.89 for $Cu_6Sn_5$–Sn 1/4, $Cu_6Sn_5$–Sn 1/2, $Cu_6Sn_5$–Sn 1/1, and $Cu_6Sn_5$ NPs, respectively. The final Cu and Sn contents in the produced Cu–Sn NPs were calculated on the basis of the ICP-MS results in order to have a better understanding of the growth mechanism. The Sn content shows a declining trend dropping from 0.41 to 0.24 mmol (from 1/4 to 2/1 Cu/Sn feeding ratio), whereas the Cu content climbs from 0.10 to 0.46 mmol. The increase in Cu content accompanied by the decrease in Sn content suggests a galvanic replacement growth mechanism, in which the metallic Sn atoms reduce Cu ions and are replaced by reduced Cu atoms. The galvanic replacement is driven by the different electrochemical reduction potentials, in which the metal with low reduction potential reduces the ion of the metal with high reduction potential.[28] As shown in eqs 1 and 2, the reduction potential of Sn is lower than Cu. Therefore, the Sn in the Sn NPs can reduce the $Cu^{2+}$, through which the oxidized Sn leaves the original position and is replaced by the reduced Cu.

$$Sn^{2+} + 2e^- \rightarrow Sn \; E^0 = -0.14 \text{ V vs RHE} \tag{1}$$

$$Cu^{2+} + 2e^- \rightarrow Cu \; E^0 = +0.34 \text{ V vs RHE} \tag{2}$$

The chemical states of Cu and Sn in hybrid $Cu_6Sn_5$–Sn and $Cu_6Sn_5$ NPs were characterized by X-ray photoelectron spectroscopy (XPS). Figure S3a shows that the majority of the surface Sn from both $Cu_6Sn_5$–Sn 1/1 and $Cu_6Sn_5$ NPs are Sn(IV) species. A small fraction of Sn(0) was found from both samples as well, 33% for $Cu_6Sn_5$–Sn 1/1 and 18% for $Cu_6Sn_5$ NPs. Sn $M_4N_{45}N_{45}$ Auger signal was also collected to assist in identifying Sn(IV) species. To determine the chemical state of Cu, Cu 2p core level, and Cu $L_3M_{45}M_{45}$ Auger signals were collected (see Figure S3b, c). The Wagner plot of Cu was also presented in Figure S3d. The data points from both samples are close to the one for metallic Cu and away from those for $Cu_2O$ and CuO. This is consistent with Cu interacting with Sn and forms intermetallic species without ionic bonding. Quantitative analysis of XPS peak intensity shows Sn enrichment on the surface. The relative sensitivity factor (RSF)-corrected intensity ratio between Sn and Cu is 94:6 for $Cu_6Sn_5$–Sn 1/1 and 76:24 for $Cu_6Sn_5$ NPs. The surface richness in Sn(IV) species is most likely due to the oxidation of
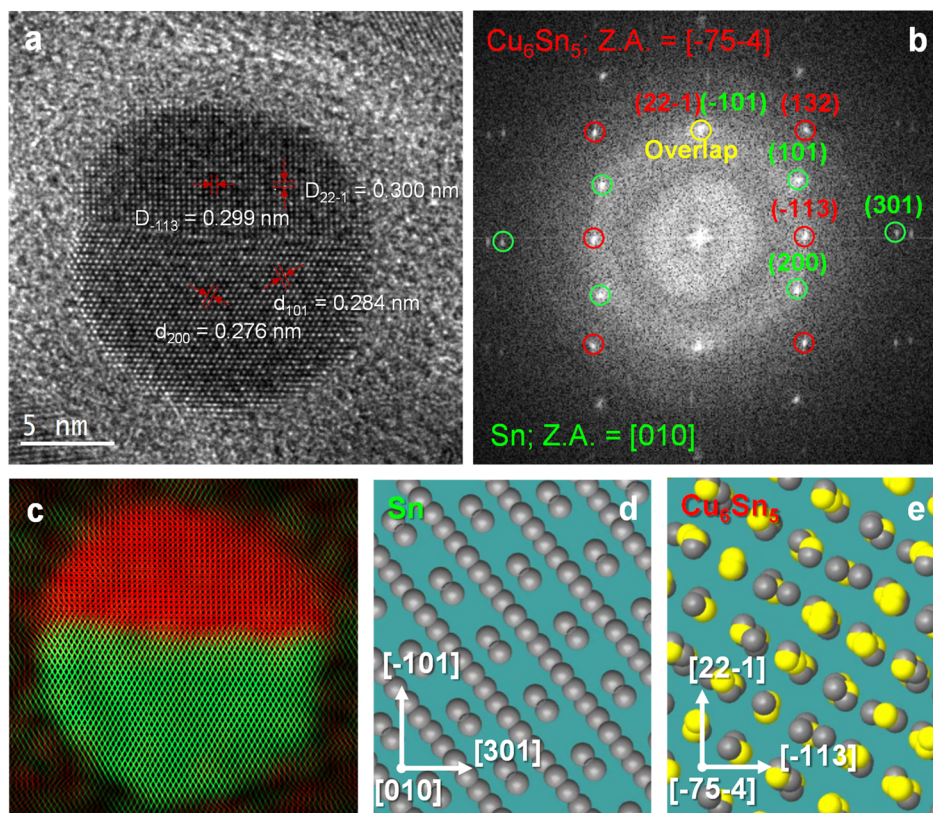
**Figure 3.** HR-TEM analysis of hybrid $Cu_6Sn_5$−Sn 1/2 NPs: (a) HR-TEM image of a hybrid $Cu_6Sn_5$−Sn NPs; (b) FFT of image a showing the coexistence of $Cu_6Sn_5$ and Sn lattice diffraction spots; (c) color mixing image from inverse FFT images using the Sn (green) and $Cu_6Sn_5$ (red) lattice spots; (d, e) crystal model of Sn and $Cu_6Sn_5$.

Sn from air exposure of the sample during preparation and transfer.[26]

The nitrate electroreduction reaction was used to evaluate the catalytic properties of these hybrid $Cu_6Sn_5$−Sn NPs. We used a nitrate alkaline solution (0.1 M $KNO_3$ + 1 M KOH) as the electrolyte in a five-neck electrochemical cell. The Cu−Sn NP/Vulcan loaded on a rotating disk electrode (RDE) was used as the working electrode, and Pt mesh and Hg/HgO electrodes were used as the counter and reference electrodes, respectively. Under He protection, the catalysts were activated with the linear sweep voltammetry (LSV) from 0.3 V to −0.5 V vs RHE. The catalytic activities of the nitrate electroreduction reaction on different bimetallic Cu−Sn and Sn NPs were then inspected by LSV from 0.3 to −0.2 V vs RHE with 400 rpm rotating rate of RDE. The current in the LSV profile was normalized by the total amount of metal (mass of Sn + Cu). The bimetallic Cu−Sn NP catalysts show the onset potential (potential at 10 mA mg$^{-1}$ current) at around 0.2 V vs RHE followed by a sharply increased current. Unlike the bimetallic catalysts, Cu/Vulcan has a more negative onset potential at 0.130 V vs RHE and a slowly increased current. The Sn NPs show a negligible current (6.1 mA mg$^{-1}$) within the tested potential range, as shown in Figure 4. Among all bimetallic Cu−Sn catalysts, the hybrid $Cu_6Sn_5$−Sn 1/1 NPs show the best activity with an onset potential at 0.214 V vs RHE and a current of 1125 mA mg$^{-1}$ at −0.2 V vs RHE. The most Sn-rich catalyst, hybrid $Cu_6Sn_5$−Sn 1/4 NPs, shows the most negative onset potential (0.197 V vs RHE) and lowest mass activity (923 mA mg$^{-1}$) at −0.2 V vs RHE. With the increase in Cu/Sn ratio from 1/4 to 1/1, the catalytic nitrate
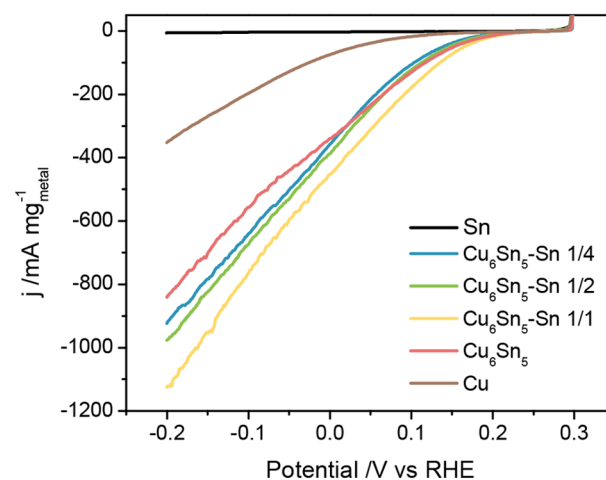


**Figure 4.** LSV profile of electroreduction of nitrate with different working electrodes. LSV condition: 0.1 M $KNO_3$ + 1 M KOH as electrolyte, 400 rpm rotating rate of RDE, 10 mV/s sweep rate with 80% IR compensation.

electroreduction activities are enhanced. Since increasing the Cu/Sn ratio enlarges the $Cu_6Sn_5$ crystal domain in hybrid NPs, we speculate that $Cu_6Sn_5$ could be the active phase for this reaction. However, with the further increase in the Cu/Sn ratio to 2/1, the catalytic activity decreases slightly, suggesting that the remaining Sn phase in the hybrid $Cu_6Sn_5$−Sn NPs could serve as a promoter to enhance the activity of $Cu_6Sn_5$. The promotion effect of Sn has also been reported on other metal catalysts, such as Pt,[29] Pd,[30] Rh,[31] and Ni.[32] Among the p-
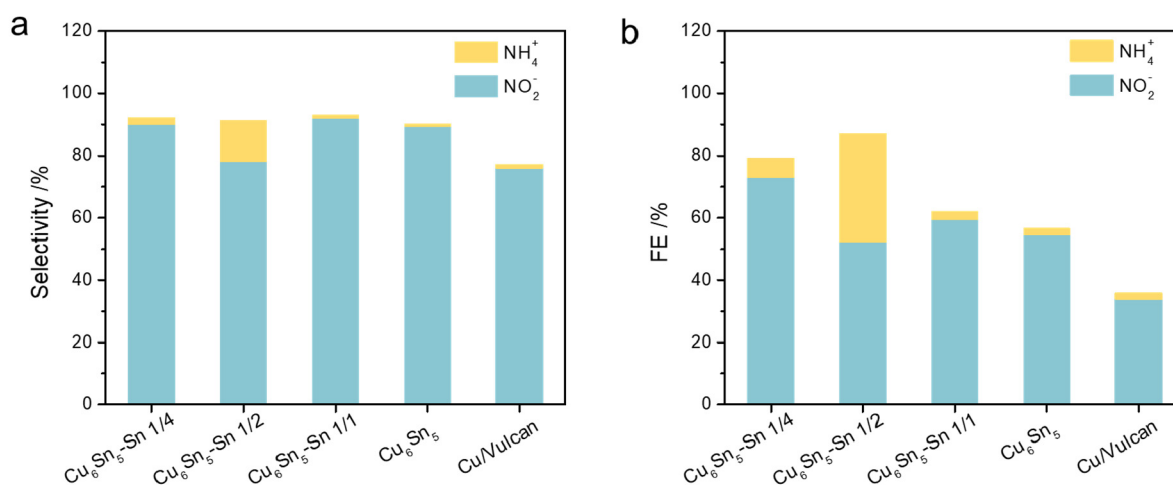
**Figure 5.** Evaluation of different Cu and Sn catalysts for nitrate electroreduction in H-cell: (a) selectivity of N species nitrite and ammonia; (b) Faradaic efficiency for the nitrate electroreduction products. Reaction condition: 12 mL 0.1 M $KNO_3$ + 1 M KOH solution in cathode, 5 h reaction under −0.2 V vs RHE, 400 rpm continuously stirring. Sn NPs were tested but showed negligible conversion after 10 h under the same reaction condition.
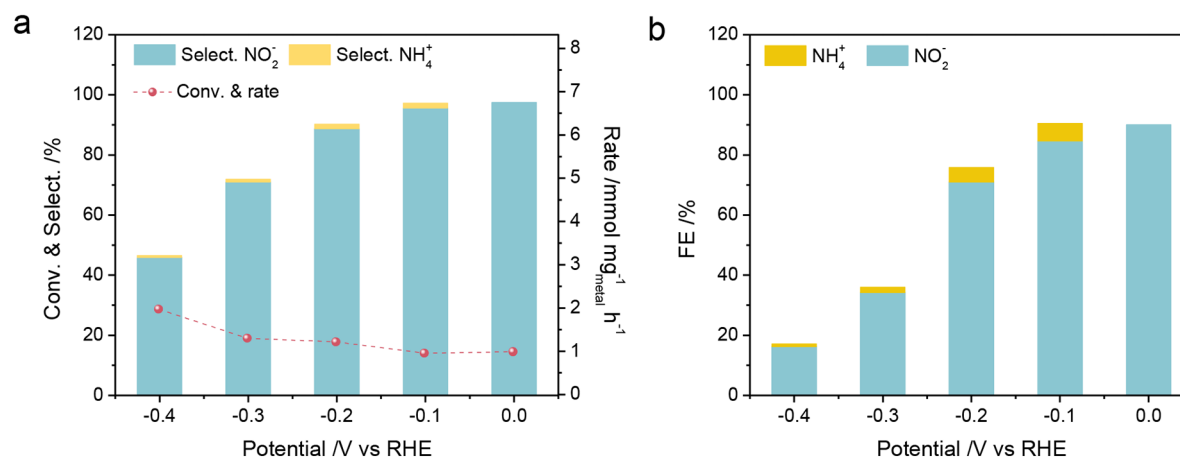
**Figure 6.** Catalytic properties of hybrid $Cu_6Sn_5$−Sn 1/1 NPs for nitrate electroreduction reaction under different potentials: (a) conversion and rate of nitrate reduction and selectivity of the products; (b) FEs for the products of the nitrate electroreduction reaction. Reaction condition: 12 mL 0.1 M $KNO_3$ + 1 M KOH solution in cathode, 2 h reaction, 400 rpm continuously stirring.

block metals, Sn was discovered as the best promoter for Pt in electroreduction of nitrate in acid media with significantly improved activity.[33] The as-synthesized hybrid $Cu_6Sn_5$−Sn NPs exhibit the top performance of nitrate electroreduction with a low energy barrier (positive onset potential) and high activity (sharp current increase) compared to the state-of-the-art catalysts.[20,22,23,34]

The possible competition hydrogen evolution reaction during nitrate electroreduction was tested in 1 M KOH solution (Figure S4). For all the tested samples, the current of the hydrogen evolution reaction is lower than 5 mA mg$^{-1}$ at −0.2 V vs RHE. This current is less than 1% of the current in nitrate electroreduction with the bimetallic Cu−Sn NPs. The electrochemical surface area (ECSA) was evaluated by measuring the double-layer capacitance in 1 M KOH (Figure S5). The double-layer capacitances of the Sn and the hybrid $Cu_6Sn_5$−Sn NPs are similar, which are 26.67 mF mg$^{-1}$ for Sn NPs and 25.40, 25.86, and 25.25 mF mg$^{-1}$ for hybrid $Cu_6Sn_5$−Sn 1/4, 1/2, and 1/1 NPs, respectively. The Cu/Vulcan sample has the highest double-layer capacitance of 66.69 mF

mg$^{-1}$. Hence, the ECSA analysis suggests that the larger nitrate reduction currents of the hybrid $Cu_6Sn_5$−Sn and $Cu_6Sn_5$ NPs than that of Cu/Vulcan originate from the higher activity of active sites instead of the influence of their surface areas.

To quantify nitrate electroreduction products and Faradaic efficiency (FE), we evaluated the reaction in an H-cell with catalysts loaded on 1 cm$^2$ carbon fiber paper as the working electrode. The performance of the as-synthesized Cu−Sn NPs and Cu/Vulcan catalyst in nitrate electroreduction was screened under −0.2 V vs RHE for 5 h, and the electrolyte was collected for the product analysis. For Sn NPs, the conversion of nitrate electroreduction is too low to be detected by high-performance liquid chromatography (HPLC) after a 10 h reaction. To eliminate the influence of the possible N-species in the reaction system on the results, we performed a blank test at −0.2 V vs RHE under nitrate-free electrolyte (1 M KOH) with $Cu_6Sn_5$−Sn 1/1 NPs as working electrode. No nitrate, nitrite, or ammonia was detected after 10 h reaction. The selectivities of nitrate electroreduction with Cu and different Cu−Sn catalysts are shown in Figure 5a, where nitrite

is identified as the primary product. Nitrite is an important chemical in industry, participating in the synthesis of many pharmaceutical and agricultural products.[24] $Cu_6Sn_5$−Sn 1/4, $Cu_6Sn_5$−Sn 1/1, and pure phase $Cu_6Sn_5$ NPs show ~90% nitrite selectivity, whereas hybrid $Cu_6Sn_5$−Sn 1/2 NPs and Cu/Vulcan reaches only ~76% selectivity to nitrite. Figure 5b shows the calculated FEs for products of nitrate electroreduction reaction. The FE of hybrid $Cu_6Sn_5$−Sn 1/4 NPs is the best, 73% for nitrite. With the increase in the Cu/Sn ratio, the FE for nitrite declines, and the pure Cu catalyst shows only 34% of the FE for nitrite. In nitrate electroreduction reaction, the reduction of nitrate to nitrite is considered as the rate determining step (RDS).[25] The produced nitrite in the RDS quickly converts to NO and further reduces to two major products, nitrogen and ammonia. The high nitrate reduction activity for hybrid $Cu_6Sn_5$−Sn NPs, large current and small onset potential, implies that the RDS is effectively overcome, whereas the reduction reaction stops at the nitrite. This phenomenon is different from noble metal[35] and some reported Cu-based catalysts[36] in the nitrate electroreduction reaction. These catalysts are usually less active (more negative onset potential and low current density) and produce dinitrogen or ammonia as the major products, indicating slow rates on the nitrite formation step but rapid nitrite conversion to the stable N-species.

To have a deep understanding of the hybrid $Cu_6Sn_5$−Sn NPs as the catalysts for nitrate electroreduction to product nitrite, we performed the reaction under a range of potentials from 0 to −0.2 V vs RHE. More negative potentials (−0.3 and −0.4 V vs RHE) were also involved in studying the potential effect on the product selectivity. We chose the hybrid $Cu_6Sn_5$−Sn 1/1 as the object of study, which shows the moderate selectivity and FE for nitrite at −0.2 V vs RHE. To prevent the over reduction of nitrite, we kept the reaction time at 2 h, at which the nitrate conversion is less than 30%. As shown in Figure 6, the hybrid $Cu_6Sn_5$−Sn 1/1 NPs exhibits the best selectivity (97%) and the highest FE (90%) for nitrite at 0 V vs RHE. With more negative potential, the conversion of nitrate increases, whereas both selectivity and FE of nitrite decrease. As the potential decreased from 0.0 to −0.4 V vs RHE, the corresponding reaction rate increased from 1 to 2 mmol $mg^{-1}_{metal}$ $h^{-1}$, respectively. A detailed mechanistic study about nitrate electroreduction on Cu electrode in alkaline solution reports that nitrite is the major product of nitrate electroreduction at 0 V vs RHE, whereas the nitrite species was reduced to a hydroxylamine intermediate that immediately reduces to ammonia under the potential more negative than −0.2 V vs RHE.[37] Agreeing with this previous study, our nitrate electroreduction results on hybrid $Cu_6Sn_5$−Sn NPs catalysts show that nitrite becomes the major product at more positive potentials. Unlike Cu, the hybrid $Cu_6Sn_5$−Sn NPs maintain the high nitrite selectivity at −0.2 V and even more negative potentials. The enhanced selectivity to nitrite at more negative potentials on hybrid $Cu_6Sn_5$−Sn NPs could be due to more negative potential for nitrite than nitrate reduction or weakened adsorption of nitrite. The weak adsorption of nitrite could lead to the release of nitrite from the catalyst surface immediately after being produced, preventing further reduction. In addition, the recycle test shows as-synthesized $Cu_6Sn_5$−Sn NPs kept good selectivity to nitrite with moderate deactivation, as shown in Figure S6.

An electroreduction of the nitrite experiment was performed to confirm the wide onset potential window between the electroreduction of nitrate and nitrite. From Figure S7, compared with the electroreduction of nitrate, a more negative onset potential of nitrite electroreduction (0.062 V vs RHE) and lower mass activity (384 mA $mg^{-1}$ at −0.2 V vs RHE) suggests that the hybrid $Cu_6Sn_5$−Sn NPs can catalyze electroreduction of nitrite, but less active. In addition, the products of electroreduction of nitrite were examined after 5 h of reaction with hybrid $Cu_6Sn_5$−Sn 1/1 NPs as the catalysts. Table S2 shows the comparison of nitrate and nitrite electroreduction under similar conditions. The conversion of nitrite electroreduction is lower than the nitrate electroreduction. The electroreduction reaction results provide evidence to support the possibility of obtaining high selectivity to nitrite on hybrid $Cu_6Sn_5$−Sn NPs at appropriate potentials.

## CONCLUSION

In conclusion, a one-pot, two-step hot injection method was developed to prepare monodisperse anisotropic nanomaterials, hybrid $Cu_6Sn_5$−Sn intermetallic−metal NPs. The components of the bimetallic Cu−Sn NPs were precisely controlled from hybrid to pure phase NPs by tuning the reaction condition. Galvanic replacement was proposed as the growth mechanism after careful characterizing hybrid NPs with TEM, XRD, and ICP-MS. The as-synthesized hybrid $Cu_6Sn_5$−Sn NPs show promising catalytic activity on the nitrate electroreduction reaction with positive onset potential and high current. With the modification of Sn, the hybrid $Cu_6Sn_5$−Sn NPs exhibit high selectivity in the production of an unstable intermediate, nitrite, within a wide range of potentials. The demonstrated synthetic method and the growth mechanism could be extended to the controllable synthesis of other intermetallic or hybrid intermetallic−metal NPs with unique properties applicable to various fields.

## EXPERIMENTAL SECTION

**Materials.** Lithium bis(trimethylsilyl)amide ($LiN(SiMe_3)_2$, 97%, Aldrich), oleic acid (OA, 90%, Aldrich), tin(II) chloride ($SnCl_2$, anhydrous, 98%, BTC), tetrachloroethylene (TCE, ≥ 99%, Aldrich), diisobutylaluminum hydride (DIBAH, 1.0 M solution in THF, Aldrich), oleylamine (OAm, techn., TCI), copper acetylacetonate ($Cu(acac)_2$, ≥ 99%, Merck KGaA), potassium hydroxide (KOH, 86.4%, Fisher Chemical), potassium nitrate ($KNO_3$, 100.0%, Fisher Chemical), potassium nitrite ($KNO_2$, 97%, Acros Organics), Nafion perfluorinated resin solution (5 wt % in lower aliphatic alcohols and water, Aldrich), and Vulcan XC-72 (Cabot) were used as received. All synthesis operations were carried out under a vacuum or using an argon Schlenk line.

**Synthesis of the Bimetallic Cu−Sn NPs.** Bimetallic Cu−Sn NPs were synthesized through a hot injection method. Typically, in a 100 mL three-neck flask, 20 g of OAm was degassed at 140 °C under a vacuum for 1.5 h. After being cooled to 50 °C, 0.5 mmol $SnCl_2$ was added. The mixture was heated up to 140 °C and degassed for another 30 min, following by backfilling argon. In parallel, the $LiN(SiMe_3)_2$/toluene solution was prepared in a glovebox, during which 1.204 g of $LiN(SiMe_3)_2$ was dissolved in 4 mL of dry toluene. At 210 °C, 2 mL of $LiN(SiMe_3)_2$/toluene solution was injected, and 0.6 mL of DIBAH/THF (1 M DIBAH in THF) solution was injected immediately. The color of the mixture turned black immediately after adding the DIBAH reductant solution. In an 80 °C oil bath, a Cu precursor solution was prepared by dissolving $Cu(acac)_2$ in OAm. After 6 h at 210 °C, the Sn NPs solution was cooled to 120 °C, and the copper precursor solution was added dropwise with an injection rate of 0.5 mL/min, which was precisely controlled by a syringe pump. The Cu−Sn mixture was kept at 120 °C for 1 h and then cooled to room temperature using a 25 °C water bath. During the cooling, 10 mL of toluene was added at 50−60 °C. The mixture was

centrifuged at 8000 rpm for 4 min and redispersed in oleic acid/TCE solution for ligand exchange. After ligand exchange, Cu−Sn NPs were precipitated by adding ethanol and centrifugation. Finally, the Cu−Sn NPs were dispersed and stored in TCE. The synthesis parameters of different Cu−Sn NPs are listed in Table S1.

Sn NPs were synthesized with a similar procedure. After 6 h of reaction at 210 °C, the mixture was directly cooled to room temperature using a water bath, followed by centrifugation and ligand exchange.

**Characterization.** Transmission electron microscopy (TEM) images were taken using a TECNAI G2 F20 operated at 200 kV. HAADF STEM imaging was performed on a Titan Themis 300 probe corrected TEM with a Super-X EDX detector. Powder X-ray diffraction (PXRD) was performed on a Bruker D8 Advance Twin diffractometer using Cu $K\alpha_1$ radiation (40 kV, 40 mA, $\lambda$ = 0.1541 nm). The ICP-MS results were obtained by Agilent 7700 ICP-MS. The samples were digested completely in boiling aqua regia.

The XPS measurements were performed using a Kratos Amicus/ESCA 3400 instrument. The sample was irradiated with 240 W unmonochromated Mg $K\alpha$ X-ray, and photoelectrons emitted at 0° from the surface normal were energy analyzed using a DuPont type analyzer. The pass energy was set at 150 eV. CasaXPS was used to process raw data. An asymmetric LA(1.2,1.5,5) line shape was used to fit Sn(0) component, and a symmetric GL(30) line shape was used to peak fit Sn(IV) component in the Sn $3d_{5/2}$ region.

**Electroreduction of Nitrate.** Preparation of Cu−Sn/Vulcan catalyst ink: Cu−Sn NPs were loaded on Vulcan XC-72, washed with the mixture hexanes and ethanol solvent three times, and dried using the Schlenk line under vacuum. To prepare the ink for the rotating disk electrode (RDE), 2 mg Cu−Sn/Vulcan was dispersed by sonication in 0.5 mL of ink solution (0.4 mL of $H_2O$, 0.1 mL of isopropanol, and 5 $\mu$L of Nafion solution). The ink for the carbon fiber electrode was prepared by dispersing 2.5 mg of Cu−Sn/Vulcan in 0.5 mL of ink solution (0.1 mL of $H_2O$, 0.4 mL of isopropanol, and 5 $\mu$L of Nafion solution).

All electrochemical data were recorded in a three-electrode system with a potentiostat (VSP- 300, Bio-Logic Science Instruments). The linear sweep voltammetry (LSV) profiles were obtained with a RDE (5 mm in diameter) deposited with 20 $\mu$L of prepared catalysis ink as the working electrode, Pt mesh as the counter electrode, and Hg/HgO (1 M KOH) as the reference electrode. The reaction system was purged by He before and during the test. For the nitrate electro-reaction test, a solution of 0.1 M $KNO_3$ + 1 M KOH was used as the electrolyte. Solutions of 1 M KOH and 1 M KOH + 0.1 M $KNO_2$ were used for the blank scan and nitrite electroreduction test, respectively. LSV tests were performed at 400 rpm rotating rate from 0.3 V to −0.2 V vs RHE with the scan rate of 10 mV/s. An 80% IR compensation was applied for all the LSV scans.

A Hg/HgO reference electrode was calibrated in 1 M KOH with hydrogen oxidation reaction (HOR), during which the Pt mesh, serving as the working electrode, was continuously exposed to hydrogen directly. The following equation was used to convert potentials to a reversible hydrogen electrode (RHE):

$$E_{RHE} = E_{Hg/HgO} + 0.059\ pH + E^0_{Hg/HgO} = E_{Hg/HgO} + 0.924$$

Electrochemical surface areas (ECSAs) were estimated by measuring the double-layer capacitance. Cyclic voltammetry (CV) was run from 0.19 to 0.29 V in 1 M KOH electrolyte under the protection of He. Different scan rates of 120, 100, 80, 60, 40, and 20 mV/s, were applied. The double-layer capacitances were calculated by plotting the current against the scan rate and performing the linear fitting.

The nitrate electroreduction reaction studies were also performed in an H-cell with 50 $\mu$L of Cu−Sn/Vulcan catalyst ink deposited on 1 $cm^2$ carbon fiber paper as the working electrode, Hg/HgO as the reference electrode, Pt mesh as the counter electrode, and Nafion212 membrane to separate the cathode and anode. The nitrate electroreduction reactions were performed at room temperature with stirring at 400 rpm under the protection of He. The current was recorded every 5 s without IR compensation, and the electrolyte was

collected for product analysis and quantification. The standard deviations in product selectivity and FE are less than 5%.

Ammonia was quantified through the indophenol colorimetry method.[38] Three solutions were prepared: (I) coloring solution: 0.4 M sodium salicylate with 0.32 M NaOH; (II) oxidation solution: sodium hypochlorite solution with 0.75 M NaOH; (III) catalyst solution: 0.1 g of $Na_2[Fe(CN)_5NO]\cdot2H_2O$ dissolved in 10 mL of $H_2O$. During the quantification of ammonia, 0.5 mL of solution I and 0.05 mL of solution II and III were added to 4 mL of electrolyte solution. After 2 h, the absorbance measurement was performed using a UV−vis spectrometer (Agilent 8453). The calibration standard was prepared with $NH_4NO_3$ in 1 M KOH solution with the range of 0 to 100 $\mu$M, and the calibration curve was plotted with absorbance at 665 nm vs ammonia concentration (Figure S8).

Nitrate and nitrite were quantified with HPLC equipped with a UV detector (Agilent 1200 Series).[38] The wavelength was fixed at 213 nm for the UV detector, and an Agilent XDB C18 (4.6 × 150 mm, 1.8 $\mu$m) column was used to separate nitrate and nitrite. The electrolyte was diluted 10 times with Milli-Q water, and 1 $\mu$L of was injected for the test. The mobile phase consists of 0.01 M n-octylamine in the mixed solvent of 30% methanol and 70% water, adjusted to pH 7 by phosphoric acid. The mobile phase was driven by a binary pump with a rate of 0.7 mL/min. The running time for each sample was set as 6 min. The retention times of nitrate and nitrite are around 3 and 5 min, respectively. The calibration curve was prepared in the range of 0.1 to 15 mM for nitrate and 0.1 to 10 mM for nitrite (Figure S9).

The conversion of nitrate and selectivity of N-species were calculated using the following equations:

$$Conversion\% = \frac{C_{nitrate,i} - C_{nitrate,t}}{C_{nitrate,i}} \times 100$$

$$Nitrite\ selectivity\% = \frac{C_{nitrite,i}}{C_{nitrate,i} - C_{nitrate,t}} \times 100$$

$$Ammonia\ selectivity\% = \frac{C_{ammonia,t}}{C_{nitrate,i} - C_{nitrate,t}} \times 100$$

where $C_{x,i}$ represents the initial concentration of $x$-species, and $C_{x,t}$ stands for the concentration of $x$-species at time $t$.

The Faradaic efficiency was calculated through the following equation:

$$FE\% = \frac{nV_{catholyte}C_xF}{It} \times 100$$

where $n$ is the number of moles of electron transfer for each mole of the product $x$; $V_{catholyte}$ is the volume of electrolyte in the cathode, 12 mL; $C_x$ represents the concentration of different products; $F$ is the Faraday constant, 96 485 C mol$^{-1}$; $I$ is current; and $t$ is the reaction time.

## ■ ASSOCIATED CONTENT

### Ⓢ Supporting Information

The Supporting Information is available free of charge at https://pubs.acs.org/doi/10.1021/acsami.1c09301.

> Scheme of 2D projection of hybrid nanoparticles; additional material characterizations (EDX mapping, XPS, ICP); stability test of nitrate electroreduction; additional electrochemical property test; calibration curves for product quantification; synthesis method and characterization of the Cu/Vulcan control catalyst (PDF)

## ■ AUTHOR INFORMATION

### Corresponding Author

**Wenyu Huang** − *Department of Chemistry, Iowa State University, Ames, Iowa 50011, United States; Ames*

Laboratory, The U.S. Department of Energy, Ames, Iowa 50011, United States; ● orcid.org/0000-0003-2327-7259; Email: whuang@iastate.edu

**Authors**

Jiaqi Yu − Department of Chemistry, Iowa State University, Ames, Iowa 50011, United States

Anna F. Kolln − Ames Laboratory, The U.S. Department of Energy, Ames, Iowa 50011, United States

Dapeng Jing − Materials Analysis and Research Laboratory, Iowa State University, Ames, Iowa 50010, United States; ● orcid.org/0000-0001-7600-7071

Jinsu Oh − Ames Laboratory, The U.S. Department of Energy, Ames, Iowa 50011, United States

Hengzhou Liu − Department of Chemical and Biological Engineering, Iowa State University, Ames, Iowa 50011, United States

Zhiyuan Qi − Chemical Sciences Division, Lawrence Berkeley National Laboratory, Berkeley, California 94720, United States; ● orcid.org/0000-0002-1495-0133

Lin Zhou − Ames Laboratory, The U.S. Department of Energy, Ames, Iowa 50011, United States; ● orcid.org/0000-0003-2286-6510

Wenzhen Li − Department of Chemical and Biological Engineering, Iowa State University, Ames, Iowa 50011, United States; ● orcid.org/0000-0002-1020-5187

Complete contact information is available at:
https://pubs.acs.org/10.1021/acsami.1c09301

**Author Contributions**

The manuscript was written through the contributions of all authors. All authors have given approval to the final version of the manuscript.

**Notes**

The authors declare no competing financial interest.

## ■ REFERENCES

(1) Yang, T.; Wei, L.; Jing, L.; Liang, J.; Zhang, X.; Tang, M.; Monteiro, M. J.; Chen, Y. I.; Wang, Y.; Gu, S.; Zhao, D.; Yang, H.; Liu, J.; Lu, G. Q. M. Dumbbell-Shaped Bi-component Mesoporous Janus Solid Nanoparticles for Biphasic Interface Catalysis. *Angew. Chem., Int. Ed.* **2017**, *56* (29), 8459−8463.

(2) Li, Z.; Rayder, T. M.; Luo, L.; Byers, J. A.; Tsung, C. K. Aperture-Opening Encapsulation of a Transition Metal Catalyst in a Metal-Organic Framework for CO2 Hydrogenation. *J. Am. Chem. Soc.* **2018**, *140* (26), 8082−8085.

(3) Sneed, B. T.; Kuo, C. H.; Brodsky, C. N.; Tsung, C. K. Iodide-mediated control of rhodium epitaxial growth on well-defined noble metal nanocrystals: synthesis, characterization, and structure-dependent catalytic properties. *J. Am. Chem. Soc.* **2012**, *134* (44), 18417−18426.

(4) Zhao, T.; Zhu, X.; Hung, C. T.; Wang, P.; Elzatahry, A.; Al-Khalaf, A. A.; Hozzein, W. N.; Zhang, F.; Li, X.; Zhao, D. Spatial Isolation of Carbon and Silica in a Single Janus Mesoporous Nanoparticle with Tunable Amphiphilicity. *J. Am. Chem. Soc.* **2018**, *140* (31), 10009−10015.

(5) Hu, H.; Liu, J.; Yu, J.; Wang, X.; Zheng, H.; Xu, Y.; Chen, M.; Han, J.; Liu, Z.; Zhang, Q. Synthesis of Janus Au@periodic

mesoporous organosilica (PMO) nanostructures with precisely controllable morphology: a seed-shape defined growth mechanism. *Nanoscale* **2017**, *9* (14), 4826−4834.

(6) Li, X.; Zhou, L.; Wei, Y.; El-Toni, A. M.; Zhang, F.; Zhao, D. Anisotropic encapsulation-induced synthesis of asymmetric single-hole mesoporous nanocages. *J. Am. Chem. Soc.* **2015**, *137* (18), 5903−5906.

(7) Zhao, T.; Chen, L.; Wang, P.; Li, B.; Lin, R.; Abdulkareem Al-Khalaf, A.; Hozzein, W. N.; Zhang, F.; Li, X.; Zhao, D. Surface-kinetics mediated mesoporous multipods for enhanced bacterial adhesion and inhibition. *Nat. Commun.* **2019**, *10* (1), 4387.

(8) Alvarez-Puebla, R. A.; Agarwal, A.; Manna, P.; Khanal, B. P.; Aldeanueva-Potel, P.; Carbó-Argibay, E.; Pazos-Pérez, N.; Vigderman, L.; Zubarev, E. R.; Kotov, N. A.; Liz-Marzán, L. M. Gold nanorods 3D-supercrystals as surface enhanced Raman scattering spectroscopy substrates for the rapid detection of scrambled prions. *Proc. Natl. Acad. Sci. U. S. A.* **2011**, *108* (20), 8157−8161.

(9) Tadesse, L. F.; Ho, C. S.; Chen, D. H.; Arami, H.; Banaei, N.; Gambhir, S. S.; Jeffrey, S. S.; Saleh, A. A. E.; Dionne, J. Plasmonic and Electrostatic Interactions Enable Uniformly Enhanced Liquid Bacterial Surface-Enhanced Raman Scattering (SERS). *Nano Lett.* **2020**, *20* (10), 7655−7661.

(10) Walther, A.; Muller, A. H. Janus particles: synthesis, self-assembly, physical properties, and applications. *Chem. Rev.* **2013**, *113* (7), 5194−261.

(11) McConnell, M. D.; Kraeutler, M. J.; Yang, S.; Composto, R. J. Patchy and multiregion janus particles with tunable optical properties. *Nano Lett.* **2010**, *10* (2), 603−609.

(12) Kamperman, T.; Trikalitis, V. D.; Karperien, M.; Visser, C. W.; Leijten, J. Ultrahigh-Throughput Production of Monodisperse and Multifunctional Janus Microparticles Using in-Air Microfluidics. *ACS Appl. Mater. Interfaces* **2018**, *10* (28), 23433−23438.

(13) Li, X.; Zhou, L.; Wei, Y.; El-Toni, A. M.; Zhang, F.; Zhao, D. Anisotropic growth-induced synthesis of dual-compartment Janus mesoporous silica nanoparticles for bimodal triggered drugs delivery. *J. Am. Chem. Soc.* **2014**, *136* (42), 15086−15092.

(14) Hu, H.; Ji, F.; Xu, Y.; Yu, J.; Liu, Q.; Chen, L.; Chen, Q.; Wen, P.; Lifshitz, Y.; Wang, Y.; Zhang, Q.; Lee, S. T. Reversible and Precise Self-Assembly of Janus Metal-Organosilica Nanoparticles through a Linker-Free Approach. *ACS Nano* **2016**, *10* (8), 7323−7330.

(15) Steimle, B. C.; Fenton, J. L.; Schaak, R. E. Rational construction of a scalable heterostructured nanorod megalibrary. *Science* **2020**, *367* (6476), 418−424.

(16) Feng, Q.; Zhao, S.; Wang, Y.; Dong, J.; Chen, W.; He, D.; Wang, D.; Yang, J.; Zhu, Y.; Zhu, H.; Gu, L.; Li, Z.; Liu, Y.; Yu, R.; Li, J.; Li, Y. Isolated Single-Atom Pd Sites in Intermetallic Nanostructures: High Catalytic Selectivity for Semihydrogenation of Alkynes. *J. Am. Chem. Soc.* **2017**, *139* (21), 7294−7301.

(17) Wang, J.; Chang, X.; Chen, S.; Sun, G.; Zhou, X.; Vovk, E.; Yang, Y.; Deng, W.; Zhao, Z.-J.; Mu, R.; Pei, C.; Gong, J. On the Role of Sn Segregation of Pt-Sn Catalysts for Propane Dehydrogenation. *ACS Catal.* **2021**, *11* (8), 4401−4410.

(18) Wang, J.; Zou, J.; Hu, X.; Ning, S.; Wang, X.; Kang, X.; Chen, S. Heterostructured intermetallic CuSn catalysts: high performance towards the electrochemical reduction of CO2 to formate. *J. Mater. Chem. A* **2019**, *7* (48), 27514−27521.

(19) Furukawa, S.; Yoshida, Y.; Komatsu, T. Chemoselective Hydrogenation of Nitrostyrene to Aminostyrene over Pd- and Rh-Based Intermetallic Compounds. *ACS Catal.* **2014**, *4* (5), 1441−1450.

(20) Wang, Y.; Xu, A.; Wang, Z.; Huang, L.; Li, J.; Li, F.; Wicks, J.; Luo, M.; Nam, D. H.; Tan, C. S.; Ding, Y.; Wu, J.; Lum, Y.; Dinh, C. T.; Sinton, D.; Zheng, G.; Sargent, E. H. Enhanced Nitrate-to-Ammonia Activity on Copper-Nickel Alloys via Tuning of Intermediate Adsorption. *J. Am. Chem. Soc.* **2020**, *142* (12), 5702−5708.

(21) Su, J. F.; Kuan, W.-F.; Chen, C.-L.; Huang, C.-P. Enhancing electrochemical nitrate reduction toward dinitrogen selectivity on Sn-Pd bimetallic electrodes by surface structure design. *Appl. Catal., A* **2020**, *606*, 117809.

(22) Chen, G.-F.; Yuan, Y.; Jiang, H.; Ren, S.-Y.; Ding, L.-X.; Ma, L.; Wu, T.; Lu, J.; Wang, H. Electrochemical reduction of nitrate to ammonia via direct eight-electron transfer using a copper−molecular solid catalyst. *Nat. Energy* **2020**, *5* (8), 605−613.

(23) Wang, Y.; Zhou, W.; Jia, R.; Yu, Y.; Zhang, B. Unveiling the Activity Origin of a Copper-based Electrocatalyst for Selective Nitrate Reduction to Ammonia. *Angew. Chem., Int. Ed.* **2020**, *59* (13), 5350−5354.

(24) Laue, W.; Thiemann, M.; Scheibler, E.; Wiegand, K. W. Nitrates and Nitrites. In *Ullmann's Encyclopedia of Industrial Chemistry*; Wiley−VCH, 2000.

(25) Duca, M.; Koper, M. T. M. Powering denitrification: the perspectives of electrocatalytic nitrate reduction. *Energy Environ. Sci.* **2012**, *5* (12), 9726−9742.

(26) Kravchyk, K.; Protesescu, L.; Bodnarchuk, M. I.; Krumeich, F.; Yarema, M.; Walter, M.; Guntlin, C.; Kovalenko, M. V. Monodisperse and inorganically capped Sn and Sn/SnO2 nanocrystals for high-performance Li-ion battery anodes. *J. Am. Chem. Soc.* **2013**, *135* (11), 4199−4202.

(27) Ma, T.; Wang, S.; Chen, M.; Maligal-Ganesh, R. V.; Wang, L.-L.; Johnson, D. D.; Kramer, M. J.; Huang, W.; Zhou, L. Toward Phase and Catalysis Control: Tracking the Formation of Intermetallic Nanoparticles at Atomic Scale. *Chem.* **2019**, *5* (5), 1235−1247.

(28) Sun, Y.; Xia, Y. Shape-Controlled Synthesis of Gold and Silver Nanoparticles. *Science* **2002**, *298* (5601), 2176−2179.

(29) Yang, J.; Duca, M.; Schouten, K. J. P.; Koper, M. T. M. Formation of volatile products during nitrate reduction on a Sn-modified Pt electrode in acid solution. *J. Electroanal. Chem.* **2011**, *662* (1), 87−92.

(30) Kato, M.; Okui, M.; Taguchi, S.; Yagi, I. Electrocatalytic nitrate reduction on well-defined surfaces of tin-modified platinum, palladium and platinum-palladium single crystalline electrodes in acidic and neutral media. *J. Electroanal. Chem.* **2017**, *800*, 46−53.

(31) Siriwatcharapiboon, W.; Kwon, Y.; Yang, J.; Chantry, R. L.; Li, Z.; Horswell, S. L.; Koper, M. T. M. Promotion Effects of Sn on the Electrocatalytic Reduction of Nitrate at Rh Nanoparticles. *ChemElectroChem* **2014**, *1* (1), 172−179.

(32) Shih, Y.-J.; Wu, Z.-L. Electroplating of surfactant-modified tin catalyst over a nickel foam electrode (Sn/Ni) for selective N2 yield from nitrate reduction as affected by Sn(200) and Sn(101) crystal facets. *Appl. Catal., B* **2021**, *285*, 119784.

(33) Yang, J.; Calle-Vallejo, F.; Duca, M.; Koper, M. T. M. Electrocatalytic Reduction of Nitrate on a Pt Electrode Modified by p-Block Metal Adatoms in Acid Solution. *ChemCatChem* **2013**, *5* (7), 1773−1783.

(34) Wu, Z.-Y.; Karamad, M.; Yong, X.; Huang, Q.; Cullen, D. A.; Zhu, P.; Xia, C.; Xiao, Q.; Shakouri, M.; Chen, F.-Y.; Kim, J. Y.; Xia, Y.; Heck, K.; Hu, Y.; Wong, M. S.; Li, Q.; Gates, I.; Siahrostami, S.; Wang, H. Electrochemical ammonia synthesis via nitrate reduction on Fe single atom catalyst. *Nat. Commun.* **2021**, *12* (1), 2870.

(35) Estudillo-Wong, L. A.; Arce-Estrada, E. M.; Alonso-Vante, N.; Manzo-Robledo, A. Electro-reduction of nitrate species on Pt-based nanoparticles: Surface area effects. *Catal. Today* **2011**, *166* (1), 201−204.

(36) Xu, H.; Xu, H.; Chen, Z.; Ran, X.; Fan, J.; Luo, W.; Bian, Z.; Zhang, W. X.; Yang, J. Bimetallic PdCu Nanocrystals Immobilized by Nitrogen-Containing Ordered Mesoporous Carbon for Electro-catalytic Denitrification. *ACS Appl. Mater. Interfaces* **2019**, *11* (4), 3861−3868.

(37) Reyter, D.; Bélanger, D.; Roué, L. Study of the electroreduction of nitrate on copper in alkaline solution. *Electrochim. Acta* **2008**, *53* (20), 5977−5984.

(38) Chen, Y.; Liu, H.; Ha, N.; Licht, S.; Gu, S.; Li, W. Revealing nitrogen-containing species in commercial catalysts used for ammonia electrosynthesis. *Nat. Catal.* **2020**, *3* (12), 1055−1061.